Materials
Advances

PAPER

View Article Online
View Journal | View Issue

Cite this: *Mater. Adv.*, 2025, **6**, 7469

Inverse nanocomposites of polyaniline/MnO_2 nanorods for efficient production of hydrogen peroxide through electrocatalytic oxygen reduction in acidic solution

Md Yeasin Pabel, Muhammed Shah Miran and Md. Mominul Islam*

Received 28th June 2025,
Accepted 27th August 2025

DOI: 10.1039/d5ma00688k

rsc.li/materials-advances

The selective two-electron oxygen reduction reaction ($2e^-$ ORR) producing H_2O_2 through an electrocatalytic approach is an attractive alternative to the industrial anthraquinone oxidation method, enabling decentralized H_2O_2 production. This study explored the potential use of an inverse nanocomposite comprising polyaniline (PAni)-embedded α-MnO_2 nanorods for a selective $2e^-$ ORR in acidic medium. α-MnO_2, PAni, and inverse composites of α-MnO_2/PAni with different compositions were synthesized using hydrothermal, chemical oxidative polymerization, and solution sonication methods, respectively. Transmission electron microscopy, Fourier-transform infrared spectroscopy, X-ray diffraction, and X-ray photoelectron spectroscopy were employed to clarify various aspects, such as morphology, functional groups, microphase, crystallinity, *etc.*, of the prepared materials. The electrocatalytic activity of the prepared inverse nanocomposites containing minute amounts of PAni dispersed phase towards the ORR in an acidic solution was evaluated with voltammetry at a rotating ring disk electrode, while the rate of H_2O_2 production was determined through chronoamperometry and the iodometric titration method. The rod-like, inverse α-MnO_2/PAni nanocomposite catalyst performs commendably for the $2e^-$ ORR with, on average, 80% selectivity toward H_2O_2 at a production rate of 433 mmol g_{cat}^{-1} h^{-1}. A plausible mechanism for the ORR on the α-MnO_2/PAni nanocomposite in an acidic medium is discussed. These findings highlight the promise of inverse α-MnO_2/PAni nanocomposites as affordable and efficient electrocatalysts for on-site production of H_2O_2 through the ORR.

1. Introduction

Hydrogen peroxide (H_2O_2) holds considerable importance in the field of industrial chemicals, finding extensive applications across several sectors, such as paper and textile manufacturing, as well as environmental remediation.[1–6] At present, the prevailing approach utilized for H_2O_2 production is the anthraquinone oxidation (AO) process, which limits its widespread application due to high operational cost and inefficiency.[7–9] Regrettably, the process of AO leads to a significant amount of waste and necessitates a labor-intensive purification stage posing considerable technical difficulties due to the need for centralized facilities.[2,3,7–9] Moreover, the production of H_2O_2 in alkaline solutions is characterized by its inherent instability, which presents challenges in terms of its storage and transportation.[7] Therefore, there is a pressing requirement for the development of a cost-effective method for onsite synthesis of H_2O_2, especially in acidic media. A viable strategy for achieving these objectives can be identified in the electrochemical reduction of O_2 by a two-electron pathway, leading to the generation of H_2O_2.[10–15] However, electrocatalysts play a critical role in maximizing the potential of this opportunity by affecting activity and selectivity with these desirable properties, especially in an acidic medium.[12,16–18]

Researchers have mainly focused on commercially feasible catalyst-based transition metal oxides, which offer excellent catalytic activity towards the oxygen reduction reaction (ORR).[10,19–24] Among them, manganese oxides (MnO_x) have garnered significant interest due to their notable benefits, including abundance, cost-effectiveness, environmental sustainability, and substantial catalytic efficacy in facilitating the electrochemical ORR.[21–23,25–27] However, most research has focused on studying the ORR on MnO_x under alkaline conditions, indicating that MnO_x typically supports the $4e^-$ ORR.[21–23,28–30] Ohsaka *et al.* have reported that the ORR on MnOOH encompasses an electrochemical process, succeeded by the subsequent disproportionation of electrochemical reduction intermediates, specifically O_2^- and HO_2^-, resulting in a quasi $4e^-$ pathway.[23] Tang *et al.* have showed that MnO_x characterized by higher Mn valence states, like γ-MnOOH and $Mn(OH)_4$ composites, exhibits enhanced catalytic

---

Department of Chemistry, University of Dhaka, Dhaka, 1000, Bangladesh. E-mail: mominul@du.ac.bd

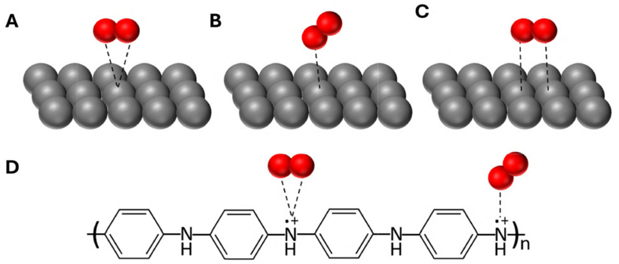

E

reactions	no. of e^-	E^0 (V *vs.* SHE)
$O_2 + 4H^+ + 4e^- \leftrightarrow 2H_2O$	4	1.23
$O_2 + 2H^+ + 2e^- \leftrightarrow H_2O_2$	2	0.70
$H_2O_2 + 2H^+ + 2e^- \leftrightarrow 2H_2O$	2	1.76

Scheme 1 (A)–(C) Possible adsorption orientation of O_2 on the catalysts: Griffiths (A), Pauling (B) and Bridge (C) modes, (D) specific interaction of O_2 with the backbone of PAni, and (E) different reaction steps involving the ORR in acidic solution.

efficiency in the ORR when contrasted with counterparts possessing lower Mn valences.[29] The catalytic activities of MnO_2 are notably affected by its crystallographic structures in the order of $\alpha > \beta > \gamma$.[21,31] Moreover, α-MnO_2 nanowires have been reported to demonstrate size-dependent functionality, where their nanoform shows a superior performance in comparison to microparticles.[30] However, the activity and selectivity of the ORR on MnO_x depend on the valence states of Mn and its crystallographic phases.[21,23,25,28–30] The mechanism of the ORR either to be $2e^-$ or $4e^-$ also depends on adsorption orientation and the binding energy of O_2 to the active sites of the catalysts,[18,20] regulating the selectivity of the ORR (Scheme 1). There are three adsorption modes for O_2 on the catalyst surface as illustrated in Scheme 1A–C. In the Griffiths mode, two oxygen atoms bind on a single site, usually leading to dissociative adsorption and water formation. The Pauling mode involves one oxygen atom binding with partial charge transfer, resulting in peroxide formation. The bridge mode is similar to the Griffiths model but requires two adsorption sites. The adsorption mode depends on the nature of the catalyst surface, while the ultimate product is influenced by both binding energy and modes of adsorption of O_2. However, there are several challenges for efficient electrochemical production of H_2O_2 using an MnO_x modified electrode in acidic medium. One challenge is the insufficient electrical conductivity of the MnO_x modified electrode because of the insulating nature of MnO_x.[25,32] Another challenge is poor adhesion of the MnO_x catalysts to the electrode surface.[25] Additionally, the concentration of O_2 is limited due to its low solubility in aqueous solution (*ca.* 1 mM) at the electrode surface.[14,15,33,34] These issues can be addressed by integrating MnO_2 with conducting polymeric materials such as polypyrrole (PPy), polythiophene, polyaniline (PAni), or poly(vinyl alcohol).[22,26,27,35–37] The electrochemically prepared MnO_2/PAni and MnO_2/PPy were studied for the ORR in Na_2SO_4 and H_2SO_4 solutions, respectively.[22,36] These studies used only the cyclic voltammetric technique and proposed a probable mechanism based solely on the observed activity. However, the specific selectivity of the ORR on MnO_2/PAni, whether it involves a $2e^-$ or $4e^-$ reduction process (Scheme 1E), remains ambiguous.

The composites of MnO_2 using a minute amount of PAni, called inverse composites,[38,39] wherein MnO_2 and PAni are the matrix phase and dispersed phase, respectively, would offer outstanding properties required for selective and efficient catalysis of the ORR for enhanced production of H_2O_2. In fact, the concept of formation of an inverse composite, an intriguing class of materials,[38] is relatively new, and it provides extreme adhesion promotion of the metal-based matrix phase, *i.e.*, MnO_2 required for developing a highly stable, robust electrode. In addition, inverse nanocomposites containing a higher MnO_2 content compared to PAni may be designed with an appropriate adsorption orientation of molecular O_2 for the selective ORR (Scheme 1D). In our previous study, the enhancement and a way of tuning the solubility of O_2 have been achieved by creating a hydrophobic micelle core that actually serves as a nest for O_2 in aqueous solutions, *e.g.*, solubility enhanced by 35-times using 24 mM sodium dodecyl sulfate surfactant.[33] Therefore, the hydrophobic polymer moiety-embedded in the inverse composites with the desired metal oxides are thus thought to potentially boost the local concentration of O_2, regulate the adsorption modes of O_2 on the catalyst surface required for selective ORR, and address the mentioned limitations of using MnO_2 as an electrode material. These features are obviously lucrative for ORR catalyst design and hence motivated us to comprehensively perform ORR on the inverse MnO_2/PAni nanocomposites.

Herein, we report, for the first time to the best of our knowledge, the synthesis and investigation of an inverse MnO_2/PAni nanocomposite for efficient and selective H_2O_2 production. This work reveals changes in the electronic structure of Mn upon incorporation of PAni, as evidenced by atomic-level characterization using XPS. The ORR activity was evaluated under static conditions using cyclic voltammetry and under hydrodynamic conditions using a rotating ring disk electrode. Additional electrochemical and kinetic insights were obtained through analysis of Tafel plots and Koutecky–Levich plots, *etc.* The nanocomposite demonstrates ~80% selectivity toward the $2e^-$ ORR pathway in acidic media, with excellent operational stability. The incorporation of PAni with MnO_2 is proposed to facilitate selective $2e^-$ ORR. These findings highlight MnO_2/PAni nanocomposites as promising electrocatalysts for on-site H_2O_2 generation. Furthermore, this approach can be extended to other oxide-polymer systems, offering new possibilities for catalyst development in the ORR and other catalytic applications.

2. Methods and materials

2.1 Chemicals

All chemicals, including potassium permanganate ($KMnO_4$) (Merck India), manganese(II) sulfate monohydrate ($MnSO_4 \cdot H_2O$) (BDH England), aniline (C_6H_5–NH_2) (Merck, India), hydrochloric acid (HCl) (RCI, Thailand), ammonium persulfate

($(NH_4)_2S_2O_8$) (Merck, India), Nafion® (Sigma Aldrich, Germany), sulfuric acid (H_2SO_4) (Merck, Germany), potassium hydroxide (KOH) (Merck, Germany), potassium chloride (KCl) (Sigma Aldrich, Germany), and potassium bromide (KBr) (Sigma Aldrich, Germany) were used as received without further purification. All aqueous solutions were prepared with deionized (DI) water (specific conductivity of 0.055 $\mu S\ cm^{-1}$, model: BOECO pure, BOE-8082060, Germany).

2.2 Synthesis of the catalysts

α-MnO_2 nanorods were synthesized by a hydrothermal method using $KMnO_4$ and $MnSO_4 \cdot H_2O$ (1 : 1.87) as precursors, following the literature with minor modification.[21] In a typical synthesis, a 30 mL aqueous solution containing 0.4 g of $MnSO_4 \cdot H_2O$ and 1.0 g of $KMnO_4$ was transferred into a 40 mL Teflon-lined stainless-steel autoclave and kept at 140 °C for 12 h. The obtained MnO_2 was finally washed with DI water several times and dried in an oven at 80 °C for 24 h. PAni was synthesized by chemical oxidative polymerization using $(NH_4)_2S_2O_8$ as the oxidizing agent under acidic conditions. Briefly, a monomer solution was prepared by adding aniline monomer to a 1.0 M HCl solution. $(NH_4)_2S_2O_8$ powder was then mixed with a 1.0 M HCl solution to form the initiator solution. The monomer and initiator solutions were then simultaneously dropped into a glass reactor, and the mixture was stirred for 8 h at 5 °C. The product was subsequently washed with DI water several times and dried in an oven at 60 °C for 24 h. α-MnO_2/PAni nanocomposites with varying percentages of PAni were prepared using the solution sonication method. The required amounts of the prepared MnO_2 and PAni were dispersed into ethanol. Subsequently, the suspensions underwent sonication for approximately 2 h. The composite was then dried at room temperature for 24 h. The percentages of PAni were 10, 15, and 20 in the MnO_2/PAni nanocomposites and are abbreviated as MnO_2/PAni-10, MnO_2/PAni-15, and MnO_2/PAni-20, respectively.

2.3 Characterizations of the materials studied

High-resolution transmission electron microscopic (HRTEM) images were obtained with a transmission electron microscope with a selected area electron diffraction (SAED) pattern; JEM-2100F operated at 200 kV field emission accelerating voltage; Tokyo, Japan. Fourier transform infrared (FTIR) spectra were recorded with a Fourier transform spectrophotometer by Frontier FT-NIR/MIR, PerkinElmer, USA in transmittance mode. The X-ray diffraction (XRD) patterns of the samples were recorded with a PANalytical X'Pert Pro diffractometer (Philips PW 1724) operating at 40 kV and 30 mA using Cu Kα_1 fitted with a scintillation detector. The surface elemental composition of the materials was determined by photoelectron spectroscopy (XPS) using a thermos scientific K-alpha X-ray photoelectron spectrometer, USA. The XPS spectra were fitted using Multipak V6.1A software, in which a Shirly background was assumed, and fitting the peaks of the experimental spectra was completed by considering a combination of Gaussian (80%) and Lorentzian (20%) distributions.

2.4 Fabrication of electrodes and electrochemical measurements

As the working electrode (WE), a glassy carbon (GC) electrode (Φ = 3 mm) was used for static voltammetric measurements, whereas a rotating ring disk electrode (RRDE), consisting of a GC disk (Φ = 4.0 mm) and Pt ring (Φ_{in} = 5.0, Φ_{out} = 7.0 mm) was used for hydrodynamic voltammetric measurements. The Ag/AgCl/KCl (sat.) electrode and spiral Pt wire were the reference and counter electrodes, respectively. An aqueous solution of 0.05 M H_2SO_4 was used as the electrolyte. Prior to each measurement either N_2 or O_2 gas was passed into the electrolyte for 15 min to obtain N_2- or O_2-saturated solution. Even N_2 or O_2 gas was flashed over the solution during the measurements. Before every measurement, WE was polished carefully with an aqueous slurry of fine alumina powder on a polishing microcloth. Then WE was ultrasonicated in DI water for 5 min to remove the remaining alumina powder. To modify the electrode, a suspension of MnO_2/PAni and 5% Nafion® solution (9 : 1 (w/w)) in ethanol was made by sonicating for 1 h. The homogeneous suspension was drop cast on the WE surface with the loading mass of *ca.* 2 mg cm^{-2} and dried under ambient conditions to achieve a uniform catalyst film. The rate of production of H_2O_2 was also measured by using chronoamperometry in a three electrode cell separated by Nafion membrane and the iodometric titration method.

3. Results and discussion

3.1 Characterization of the catalysts

Fig. 1A and B show a rod-like morphology of MnO_2 with a uniform diameter throughout its length. The average diameter (*D*) and length (*L*) of MnO_2 were *ca.* 30 and 1450 nm, respectively. The large aspect ratio (*L* to *D* ratio) of *ca.* 48 suggests that the prepared MnO_2 possesses a high surface area.[21] The fringes observed for MnO_2 with an interplanar spacing of d = 0.71 nm (Fig. 1C) corresponding to the (110) lattice planes are the characteristics of α-MnO_2 with a tetragonal structure.[40,41] The faint rings with bright spots in the SAED pattern of MnO_2 also support the tetragonal structure of the α-MnO_2 nanorods prepared,[42] as clarified further using XRD analysis (Fig. 2B). Bhat *et al.* observed that MnO_2 prepared by the hydrothermal method typically exhibits nanorods with consistent thickness along their entire lengths when compared to MnO_2 prepared through chemical methods.[40] Feng *et al.* also reported analogous structures and shapes, including urchin-like, caddice-clew-like, and nanoflower MnO_2 by hydrothermal synthesis from $MnSO_4$ as the precursor and controlled use of oxidant and solution pH.[43] On the other hand, the formation of inverse nanocomposites MnO_2/PAni can be evidenced from the image shown in Fig. 1B, wherein a smaller amount of PAni nanoparticles are dispersed over the MnO_2 nanorods and PAni chains agglomerate on the surface of the MnO_2 nanorods *via* van der Waals forces.[37] The distribution of the PAni is not homogeneous because the polarity of PAni on the surface of MnO_2 leads to intermolecular attraction and chain agglomeration.[37] However, high

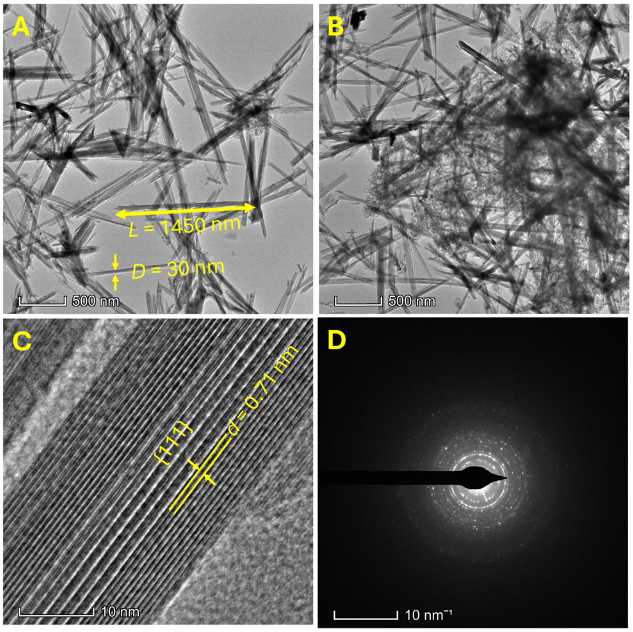

Fig. 1 (A)–(C) HRTEM images of (A) and (C) MnO_2 nanorods and (B) the MnO_2/PAni-10 inverse nanocomposite and (D) SAED pattern of the MnO_2 nanorods. Arrows and lines represent length and diameter in (A) and lattice spacing of {111} planes in (C).

molecular weight PAni forming molecular capillary bridges between MnO_2 nanoparticles can enhance the conductivity and stability of the prepared electrode. Moreover, the incorporation of a minute amount of PAni into MnO_2 will help to improve its poor adhesion with the electrode.[25]

The simplicity of the FTIR spectrum of MnO_2 (Fig. 2A-a) suggests a higher symmetry in its structure. In the far-infrared region (400–1000 cm^{-1}), the bands result from vibrations of octahedral MnO_6 units within the α-MnO_2 lattice.[41] The band at 750 cm^{-1} is specifically linked to the asymmetric stretching mode of the MnO_6 octahedral unit.[44] However, the bands at 1642 and 3450 cm^{-1} are attributed to the presence of minute amounts of water in the prepared α-MnO_2. On the other hand, the FTIR spectrum of PAni possesses distinctive bands at 1620 and 1430 cm^{-1}, as shown in Fig. 2A-b and c, corresponding to the C═C stretching vibrations of the benzenoid and quinonoid rings in PAni.[26,37] The band around 1142 cm^{-1}, attributed to C–N stretching, serves as a characteristic indicator of the conductivity of PAni, particularly in its emeraldine salt form.[37] Furthermore, the observed bands at 2912 and 2852 cm^{-1} are signatures of the formation of hydrogen bonding inside the PAni phase.[37] The spectrum of α-MnO_2/PAni (Fig. 2A-c) reveals the presence of all the characteristic bands associated with both α-MnO_2 and PAni, affirming the successful preparation of the composite. The band at 520 cm^{-1} for MnO_2 in MnO_2/PAni shifted to a higher frequency region. Moreover, a new band emerges at 952 cm^{-1} in the spectrum of the MnO_2/PAni composite, as shown in Fig. 2A-c. The development of a new band, along with the observed shifting of the original bands of the constituting components, is considered as the marker of the formation of the composite.[37]

Fig. 2B shows the XRD patterns of α-MnO_2 and α-MnO_2/PAni. The peaks at 2θ = 12.5°, 17.8°, 25.5°, 28.6°, 37.4°, 41.9°, 49.7°, 55.9°, 60.1°, 65.3°, 69.3°, 72.9° and 77.4° observed for the MnO_2 nanorods (Fig. 2B-a) are for the crystal planes of (110), (200), (220), (310), (211), (301), (411), (600), (512), (002), (541), (312) and (402), respectively, of the tetragonal phase of MnO_2.[40–42] The absence of distinctive peaks associated with other phases of manganese oxides or impurities indicates the high performance of the hydrothermal method in synthesizing pristine tetragonal MnO_2. The average crystallite size (d) of α-MnO_2, calculated from the width of the (211) peak using the Scherrer formula $d = 0.9\lambda/\beta_{1/2}\cos\theta$, where λ is the X-ray wavelength, $\beta_{1/2}$ is the corrected width of the main diffraction peak at half height, and θ is the diffraction angle, was *ca.* 37 nm. In the diffraction patterns of the MnO_2/PAni composite shown in Fig. 2B-b, a slight change of the (220) peak of pure MnO_2 occurred due to the overlapping of the (200) peak of PAni. In addition, a low-intensity peak positioned at 2θ = 20° associated with the (020) plane of PAni was observed.

So far, the synthesis of inverse MnO_2/PAni nanocomposites has been successful as confirmed by the results of TEM, FTIR spectra and XRD analyses. While low-valent states of transition

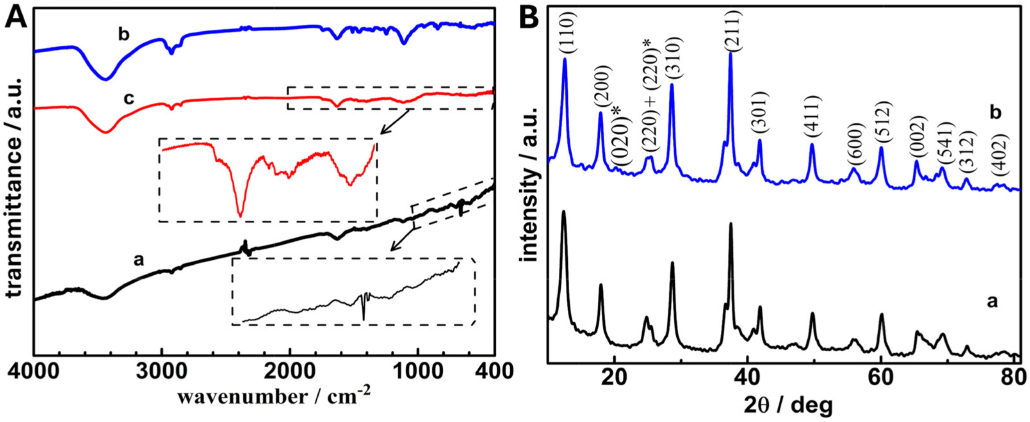

Fig. 2 (A) FTIR spectra, with the inset providing a magnified view of the selected region, and (B) XRD patterns with plane labeling (asterisks denote PAni planes) for (a) MnO_2, (b) MnO_2/PAni, and (c) PAni. a.u. on the *Y*-axes indicates arbitrary unit.

metals in catalyst families such as mixed oxides, spinels, bronzes, polyoxometalates, and metal–organic frameworks have often been associated with enhanced catalytic activity, such enhancement is typically attributed to the formation of electron-rich centers that facilitate charge transfer, generation of vacancies, electronegative doping, or synergistic effects in composite systems that enable back-donation of electrons.[25,29,45–48] However, in the case of MnO_2 for the ORR, particularly under acidic conditions, higher oxidation states of Mn are generally more favorable.[21,23,28–30] These oxidized states (*e.g.*, Mn^{4+}) provide greater structural stability, suppress Mn dissolution, and support sustained redox cycling,[21,23] whereas reduced Mn species (Mn^{2+} and Mn^{3+}) are often unstable and prone to leaching, as discussed later. In this study, the observed development of a new band and shifting of bands of the FTIR spectrum of the inverse composites direct the presence of additional electronic interaction that must be specified and quantified further. In this regard, XPS is a powerful tool to identify the elemental information that was adopted for characterization of the materials studied.[49]

Fig. 3A depicts the XPS survey spectra of MnO_2 and the inverse MnO_2/PAni nanocomposites, revealing peaks attributed to the expected elements, *i.e.*, Mn, O, C, and N. In the high-resolution XPS spectrum of Mn 2p present in pure MnO_2, two distinguishable peaks at 642.2 and 653.8 eV are observed as shown in Fig. 3B, corresponding to Mn $2p_{3/2}$ and Mn $2p_{1/2}$ of the α-MnO_2 nanorods, respectively, exhibiting a spin energy separation of 11.6 eV.[50,51] This observation aligns well with both the SAED (Fig. 1D) and XRD patterns (Fig. 2B-b), indicating the successful synthesis of α-MnO_2 nanorods. Previously, Pereira *et al.* have obtained analogous peaks at 642.2–642.25 eV and 653.8–654.05 eV for Mn $2p_{3/2}$ and Mn $2p_{1/2}$, respectively, with a spin energy separation of *ca.* 11.60 eV for α-MnO_2 nanowires.[50] On the other hand, remarkable shifting of these peaks towards higher values was observed in the case of the inverse MnO_2/PAni nanocomposites, where the peaks corresponding to Mn $2p_{3/2}$ and Mn $2p_{1/2}$ are observed at 649.8 and 661.7 eV, respectively, with a spin energy separation of 11.9 eV (Fig. 3C). These shifts in peak position towards higher energy levels, along with the increased spin energy separation, are likely attributable to the phenomenon of back donation of the electron from MnO_2 to PAni.[52] Such an electron transfer prompts a redistribution of electron density around the metal ions, leading to a stronger electrostatic attraction between the Mn 2p electrons and the nucleus of Mn, consequently shifting the binding energy of the electrons to higher energy levels.[49] It is also plausible that the interaction with PAni may not be uniform across all the orbitals of Mn in the composite, resulting in a larger apparent spin energy separation. Fig. 3D shows the high resolution XPS spectrum of N 1s present in PAni of the MnO_2/PAni nanocomposite exhibiting three peaks at 399.5,

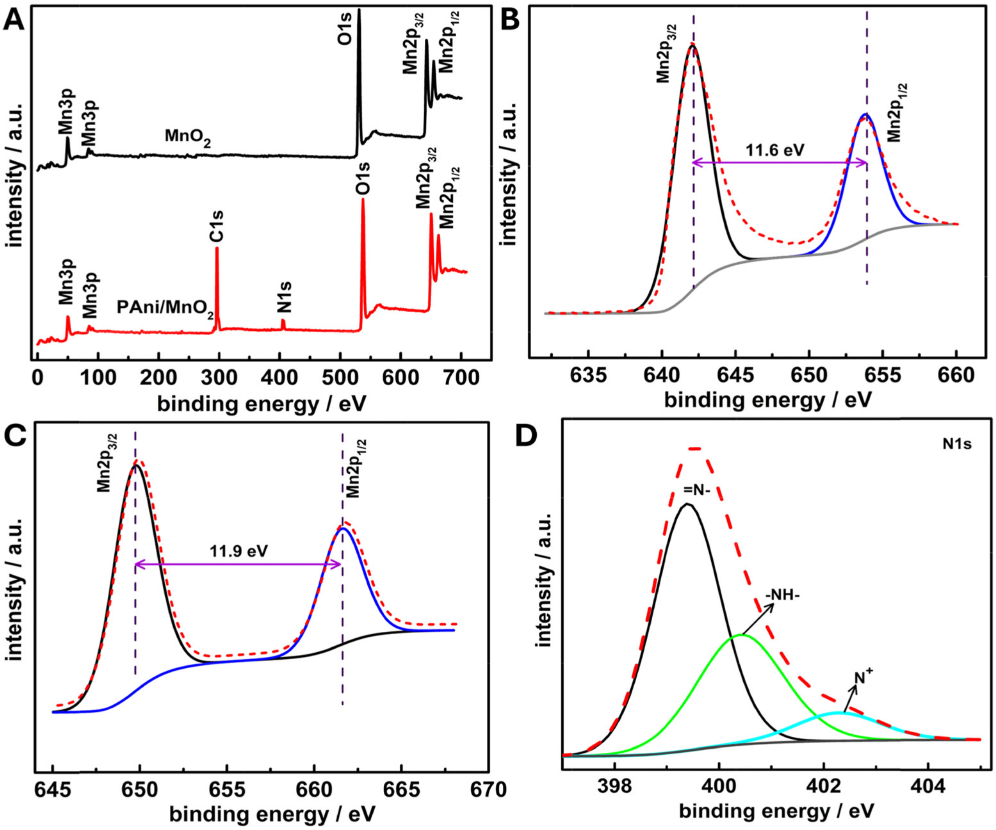

Fig. 3 (A) XPS survey spectra of MnO_2 and MnO_2/PAni. High-resolution spectra of Mn 2p of (B) MnO_2 and (C) MnO_2/PAni, and (D) N 1s of MnO_2/PAni. The perpendicular dotted lines and arrows in (B) and (D) indicate the binding energy separation of the corresponding peaks. a.u. on the *Y*-axes indicates arbitrary unit.

400.8 and 402.2 eV, corresponding to the quinoid imine, benzenoid imine and positively charged imine, respectively.[53,54] The presence of different electronic states of N was also supported by the FTIR spectrum (Fig. 2A). These observations suggest that PAni is in a protonated state. The presence of PAni in MnO_2 could serve a dual purpose: firstly, aiding in the adsorption of hydrophobic O_2 on the surface of the catalyst, and secondly, enhancing the activity and selectivity of the $2e^-$ ORR.

3.2 ORR performance of the catalysts

Fig. 4A shows the cyclic voltammograms (CVs) for the ORR and a representative corresponding background CV for the MnO_2, MnO_2/PAni-10, MnO_2/PAni-15 and MnO_2/PAni-20-modified GC electrodes. In all cases, the characteristic cathodic peaks were observed for the ORR in the presence of O_2 with a well-defined shoulder at *ca.* −0.70 V for the hydrogen evolution reaction (HER).[14,15] No anodic peak was noticed in the reverse scan, as generally not observed for the ORR in aqueous solution, *i.e.*, the ORR is an irreversible process.[14] However, as the amount of PAni in the nanocomposite increased, the onset potential shifted to the positive direction, accompanied by an increase in peak current. The number of electrons involved in the ORR is clarified later, but the possible rationale for the observed shifts in onset potential and increase in peak current may be attributed to the hydrophobic characteristics of the PAni surface,[33,34] as we have revealed in our previous study that the incorporation of hydrophobic species (sodium dodecyl sulfate (SDS)) can modulate the potential and solubility of O_2 in aqueous environments.[33]

The CV measurements for the ORR at all electrodes were further conducted at various potential scan rates (ν). Fig. 4B shows the plots of cathodic peak current densities (j_p) *vs.* square root of ν ($\nu^{1/2}$). These plots are linear, passing through the origin with the regression coefficients of 0.97, 0.99, 0.94 and 0.99 at MnO_2, MnO_2/PAni-10, MnO_2/PAni-15, and MnO_2/PAni-20 modified GC electrodes, respectively. Thus, the ORR studied using these inverse MnO_2/PAni composites is an irreversible, diffusion-controlled process as generally observed in aqueous solutions at metal, non-metal or modified electrodes.[14,15] However, the slopes of the straight lines (Fig. 4B) that indicate the number of electrons involved (n) in the ORR, diffusion coefficient (D_{O_2}) and saturation concentration of O_2 (C_{O_2}) varied according to the well-known Randles–Sevcik equation (eqn (1)) as follows:

$$j_p = 2.69 \times 10^5 n^{3/2} C_{O_2} (D_{O_2} \nu)^{1/2} \tag{1}$$

In general, the slopes obtained for the inverse composites are higher than that obtained with MnO_2, and its magnitude increased as the amount of PAni was increased. With the help of eqn (1), one may determine the product of the D_{O_2} and C_{O_2} from the obtained slope if the number of electrons involved is known. By considering the average number of electrons, n, involved in the ORR as 2, the values of the product of C_{O_2} and $(D_{O_2})^{1/2}$ were determined as 8.1×10^{-9}, 10.2×10^{-9}, 11.4×10^{-9}, and 12×10^{-8} mol cm^{-2} s$^{-1/2}$ for MnO_2, MnO_2/PAni-10, MnO_2/PAni-15, and MnO_2/PAni-20 modified GC electrodes, respectively, indicating enhanced solubility of O_2 with increasing PAni.[33,34] Nissim *et al.* have developed a simple and generally applicable electrochemical approach to ascertain the solubility of O_2 in a micellar system and found that C_{O_2} increased as the concentration of surfactant increases in the micellar system.[34] In our previous study, we employed cyclic voltammetry to evaluate the characteristics of the ORR in micellar environments.[33] A notable increase of C_{O_2} approximately 15-times higher compared to an H_2SO_4 solution, was achieved by using SDS in H_2SO_4 solution with a 4.5-times decreased D_{O_2}. This increased solubility of O_2 was attributed to the hydrophobic nature of the core of the micelles, potentially acting as a high-density O_2 reservoir.[33]

The cyclic voltammetric study reveals that the ORR can be carried out on the inverse MnO_2/PAni nanocomposites, and the polymeric micro-domain enhanced the solubility of O_2. To evaluate detailed catalytic features and the selectivity towards the ORR of the materials under consideration, the RRDE system was employed to quantify the number of electrons involved, Tafel slope, percentage of H_2O_2 production, *etc.*, for the ORR at the inverse α-MnO_2/PAni nanocomposites. Fig. 5A shows the characteristic linear sweep voltammograms (LSVs) for the ORR measured at different catalyst-modified GC

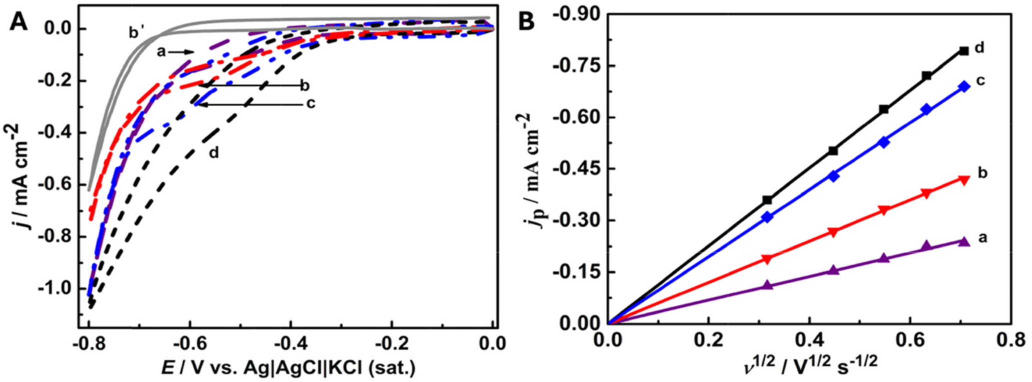

Fig. 4 (A) CVs for the ORR at (a) MnO_2, (b) and (b′) MnO_2/PAni-10, (c) MnO_2/PAni-15, and (d) MnO_2/PAni-20-modified GC electrodes in O_2- (a)–(d) or N_2-saturated (b′) 0.05 M H_2SO_4 solutions at ν of 0.10 V s^{-1}. (B) Plots of j_{pc} *vs.* $\nu^{1/2}$ obtained from CVs at various ν at the respective electrodes in O_2-saturated 0.05 M H_2SO_4.

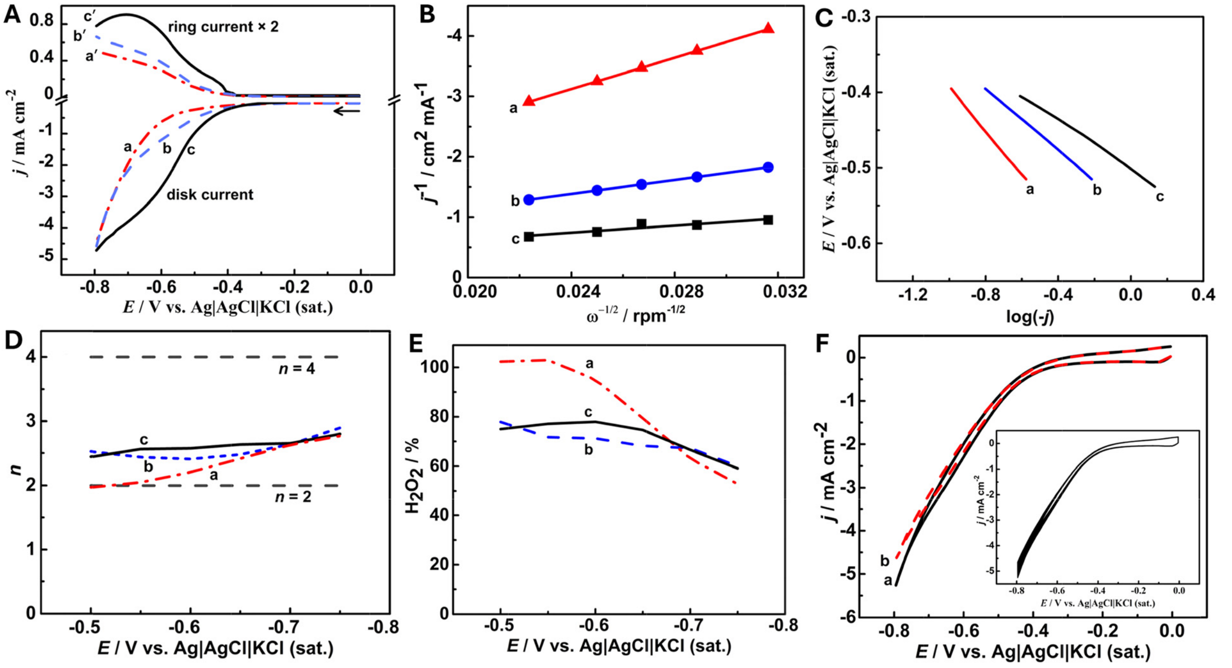

Fig. 5 Electrocatalytic ORR performances of the prepared catalysts in O_2-saturated 0.05 M H_2SO_4. (A) LSVs at a scan rate of 10 mV s^{-1} and a rotation speed of 1000 rpm. The GC disk was modified with (a) MnO_2/PAni-10, (b) MnO_2/PAni-15, (c) MnO_2/PAni-20, and the corresponding platinum ring (a′)–(c′) current. (B) *K–L* plot constructed at 0.5 V using data from LSVs recorded at various rotation rates (Fig. S3–S5). (C) Corresponding Tafel plots. (D) The electron transfer number, *n* (upper and lower dotted lines for *n* = 4 and 2, respectively). (E) Percentage of H_2O_2 selectivity obtained. (F) Initial (a) and final (b) CVs after 1000 cycles at the MnO_2/PAni-15 modified GC disk electrode at a scan rate of 10 mV s^{-1} and a rotation speed of 1000 rpm. Inset: CVs over 1000 cycles.

disks of the RRDE, where the lower set of curves refers to the oxygen reduction current and the upper set refers to the generated H_2O_2 oxidation current on a Pt ring electrode. The measured LSVs at the modified disk shown in Fig. 5A do not exhibit an oxygen reduction current reaching a diffusion-limited current plateau as observed in the corresponding CVs (Fig. 4A). This phenomenon, commonly observed in various studies under acidic conditions, suggests merging the ORR with the HER process.[14] On the other hand, the LSVs measured at the Pt ring exhibit the expected ideal shape with the current plateau occurring for the oxidation of the product generated at the disk, *i.e.*, peroxide species. However, for comparison, the current densities at 2000 rpm are shown in Fig. S1, illustrating a decreasing trend in the order of MnO_2/PAni-20 > MnO_2/PAni-15 > MnO_2/PAni-10 > MnO_2. The ring current corresponding to the MnO_2/PAni-20 disk electrode (Fig. 5A-c′) decreases with an increasing disk potential after −0.7 V. This could be attributed to the pronounced generation of hydrogen at this disk electrode, which flushes out the produced H_2O_2 beyond this potential, as indicated in the CV (Fig. 4A). The low onset potentials and reduction currents at the MnO_2/PAni modified electrodes as well as the corresponding ring current indicate a $2e^-$ pathway ORR on the catalysts, which will be further clarified later.

To evaluate the ORR kinetics at the MnO_2/PAni catalysts, the rotation-rate dependent LSVs were recorded at 800 to 2000 rpm (Fig. S2–S4). The typical Koutecký–Levich (K–L) plot of j^{-1} *vs.* $\omega^{-1/2}$ derived from the measured LSVs is presented in Fig. 5B. The good linearity and parallelism of these plots indicate the first-order kinetics with respect to molecular oxygen.[24,55] The decreasing trend of the slopes of the Tafel plots is as follows (Fig. 5C): −277 mV dec^{-1} for MnO_2/PAni-10 > −204 mV dec^{-1} for MnO_2/PAni-15 > −158 mV dec^{-1} for MnO_2/PAni-20. The values of the transfer coefficient (α) are also determined. Moreover, from the intercept of the Tafel plots, exchange current density (j_0) was estimated for evaluating the values of the standard heterogamous rate constant (k^0). The values of onset potential, E, α, j_0 and k^0 obtained for the ORR at three different electrode materials are compared in Table 1.

The value of k^0 varies when we change the ratio of metal oxide to polymer in the inverse composite, along with shifts in the onset potential (Table 1). These fluctuations of k^0 imply the existence of distinct reaction mechanisms occurring at the surface of different catalysts. The reliance of k^0 on both the onset potential and metal oxide loading again underscores the intricate nature of the ORR occurring at the MnO_2/PAni interface. At the potential region at which the ORR was studied on the composites, no potential-dependent redox reaction of PAni takes place, and only the emeraldine salt (ES) phase of PAni can persist.[56] While the structure of MnO_2 may be influenced by the applied potential in acidic environments.[57] The ES phase of PAni and the potential dependent structure of the MnO_2 rods in the composite may modulate the adsorption mode of O_2 (Scheme 1) for a selective and faster electrode reaction, producing H_2O_2 as evidenced by the enhanced ring current of the LSVs shown in Fig. 5A. Consequently, the cumulative effects of these factors,

Table 1 Different parameters of the ORR in H_2SO_4 studied at three different electrode materials

Material	E^a (V)	α	j_0 (mA cm^{-2})	$k^\circ \times 10^5$ (cm s^{-1})
MnO_2/PAni-10	0.60	0.37	0.0384	2.0
MnO_2/PAni-15	0.55	0.42	0.0323	1.7
MnO_2/PAni-20	0.50	0.34	0.2952	15.0

[a] V *vs.* Ag/AgCl.

either individually or in combination, may contribute to the observed variations in k^0. The mechanism of this catalytic performance of the composites towards the ORR and the selectivity towards high percent production of H_2O_2 were revealed by analysis of the LSVs using eqn (2) and (3).

$$n = \frac{4i_d}{i_d + \frac{i_r}{N}} \tag{2}$$

$$H_2O_2\ (\%) = \frac{200 \times \frac{i_r}{N}}{i_d + \frac{i_r}{N}} \tag{3}$$

where i_d, i_r, and N are the disk current, ring current, and collection efficiency of the ring electrode, respectively. It is clear that the values of n varied with the electrode potentials (Fig. 5D). Thus, the number of electrons involved in the ORR depends on the applied potential for all nanocomposites studied, which is common with other reported results.[5] The average n associated with the ORR at MnO_2/PAni-10, MnO_2/PAni-15, and MnO_2/PAni-20 is 2.3, 2.5, and 2.6, respectively (Fig. 5D). Generally, the ORR on MnO_2 in alkaline media involves a mediation process, where Mn(IV) undergoes reduction to Mn(III), followed by the electron transfer from Mn(III) to O_2.[21,23,58] Ohsaka *et al.* have observed that the ORR on MnOOH in alkaline solutions undergoes complicated steps of electrochemical reaction followed by subsequent disproportions of electrochemical reduction intermediates such as O_2^- and HO_2^-.[23] Generally, the oxygen reduction on MnO_2 has been proposed to follow different reactions as expressed by eqn (4)–(6).[21,23,58]

$$MnO_2 + H_2O + e^- \leftrightarrow MnOOH + OH^- \tag{4}$$

$$MnOOH + O_2 \leftrightarrow MnOO\cdots O_{2(ads.)} \tag{5a}$$

$$2MnOOH + O_2 \leftrightarrow 2(MnOOH\text{–}O_{(ads.)}) \tag{5b}$$

$$MnOOH\cdots O_{2(ads.)} + e^- \leftrightarrow MnO_2 + HO_2^- \tag{6a}$$

$$2(MnOOH\cdots O_{(ads.)}) + 2e^- \leftrightarrow 2MnO_2 + 2OH^- \tag{6b}$$

The overall reaction of eqn (4), (5a) and (6a) results in a $2e^-$ reduction process, while the combination of eqn (4), (5b) and (6b) results in an overall $4e^-$ transfer. These two schemes differ in the manner of O_2 adsorption. Cheng *et al.* have reported that both processes could occur on MnO_2, depending on the structure of MnO_2.[21] Moreover, the surface structure of PAni changes with pH, and under acidic conditions it mainly exists in the protonated ES form, which is more conductive and active.[59] This helps improve ORR performance (reaction (7)), but the exact surface changes during the reaction are still not fully understood and need further investigation. The ES phase of PAni reacts with MnO_2 to form MnOOH and pernigraniline (PN) as shown in eqn (7).[22] Consequently, at the MnO_2/PAni surface, reaction (4) could be replaced by the following reaction (7). Furthermore, Khomenko *et al.* have suggested that during the ORR on a PPy-modified graphite electrode, O_2 molecules can interact with electron-donor N atoms in PPy as well as with MnOOH (reaction (8)).[23,35,58] In the acidic medium, HO_2^- is stable and desorbs from the catalyst surface.[23]

$$([C_6H_4NH]_2[C_6H_4N]_2)_n(\text{PAni-ES}) + MnO_2 \leftrightarrow MnOOH + (C_6H_4N)_n(\text{PAni-PN}) \tag{7}$$

$$\text{PAni}\cdots O{=}O\cdots HOOMn \leftrightarrow HO_2^- + \text{PAni} + MnO_2 \tag{8}$$

The percentage of H_2O_2 production at different electrodes for different potentials is shown in Fig. 5E. It has been observed that the percentage of H_2O_2 production is also dependent on the applied voltage.[5] The number of electrons involved and the selectivity of H_2O_2 exhibit a continuous increase at increasingly negative potentials (Fig. 5D and E), suggesting a gradual reduction of the generated H_2O_2 to H_2O at the electrode surfaces. However, the average values of selectivity to H_2O_2 production in the potential range of −0.5 to −0.75 V for MnO_2/PAni-10, MnO_2/PAni-15, and MnO_2/PAni-20 are equal to 82, 71, and 70%, respectively, demonstrating a high-percentage production of H_2O_2. Table S1 compares the variations of these characteristic parameters of the ORR studied with different catalysts in both acidic and basic solutions. A notable trade-off is observed between the ORR kinetics and H_2O_2 selectivity across the MnO_2/PAni composites. While increasing the PAni content enhances the apparent electron transfer rate (Fig. 5A and Table 1), it does not lead to a proportional increase in H_2O_2 selectivity (Fig. 5E). This suggests that the conductive polymer, beyond a certain threshold, may alter the local electronic structure or adsorption environment at the MnO_2 interface, affecting the binding modes of oxygen intermediates and shifting the reaction pathway. These results highlight the necessity of optimizing the composite architecture to simultaneously maintain efficient electron transfer and high selectivity toward the $2e^-$ ORR pathway. Efficient H_2O_2 production was also confirmed by chronoamperometric measurements in a two-compartment cell (Fig. S5), and the produced H_2O_2 was determined by iodometric measurements. The calculated result shows that the production rate of H_2O_2 is 433 mmol g_{cat}^{-1} h^{-1} at the MnO_2/PAni-15 modified GC electrode in O_2-saturated 0.05 M H_2SO_4 solution.

The catalytic stability is a key factor in catalytic performance. In acidic media, MnO_2 is first reduced to MnOOH (Mn^{3+}) *via* proton insertion and electron uptake (reaction (4)),[21] and this unstable Mn^{3+} species then either reacts with O_2 (reactions (5) and (6))[23,58] or undergoes disproportionation, yielding soluble Mn^{2+} and regenerating MnO_2, leading to dissolution.[60] However, in low-concentration acid (0.05 M H_2SO_2), proton activity is reduced, slowing the dissolution pathways (reaction (4)). Additionally, PAni acts as a redox mediator (reaction (7)), stabilizing Mn valence states and preventing Mn^{3+} buildup, while its protonated ES form buffers local acidity, together effectively suppressing Mn^{2+} leaching during cycling.[27] Fig. 5F illustrates the initial (a) and final (b) CVs of the MnO_2/PAni-15 modified GC electrodes after undergoing 1000 cycles (inset of Fig. 5F) in an O_2-saturated 0.05 M H_2SO_4 solution. The cyclic voltammetric studies were performed at a scan rate of 10 mV/s and a rotation speed of 1000 rpm. The absence of a discernible peak in the CV can be attributed to the experimental conditions, specifically the dynamic environment and the utilization of a large electrode surface. During the measurement, the half-wave potential exhibits minimal change, with only a small reduction in diffusion-limiting currents. This property can be ascribed to the interaction between the catalyst and the electrode as well as the protective nature of PAni in acidic solutions.[27] Zhang *et al.* also reported the stability of PAni/MnO_2/MWCNTs in acidic solutions, attributing this stability to the protective coating of PAni.[27]

4. Conclusions

An inverse α-MnO_2/PAni nanocomposite was successfully synthesized and employed as a catalyst for the ORR in acidic media. The MnO_2/PAni catalyst exhibits approximately 80% selectivity toward the $2e^-$ ORR pathway. It achieves an H_2O_2 electrosynthesis rate of 433 mmol g_{cat}^{-1} h^{-1} *via* molecular O_2 reduction. The enhanced $2e^-$ ORR performance is attributed to improved O_2 adsorption on the catalyst surface and favorable adsorption configurations involving both MnO_2 and PAni. These synergistic features underscore the potential of MnO_2/PAni inverse nanocomposites as promising candidates for tandem electrocatalytic systems,[61] wherein the *in situ* generated H_2O_2 can drive advanced oxidation processes for organic pollutant degradation in acidic media. Furthermore, this study has the potential to be extended to other pairs of oxides and polymers for preparing inverse nanocomposites, offering a promising avenue for designing catalysts not only for the ORR but also for other potential catalysis.

Conflicts of interest

The authors declare no competing financial interests or personal relationships that could have influenced the work reported in this paper.

Data availability

Supplementary information is available. See DOI: **https://doi.org/10.1039/d5ma00688k**.

In this study, XRD measurements were carried out to reveal the basic structural information and the determination indexing of the crystal planes of the materials studied. For this, the experimental X-ray diffraction patterns given in this study were matched with appropriate entries from the Powder Diffraction File database provided by the International Centre for Diffraction Data. No structural refinement was, however, conducted that would necessitate to generate a Crystallographic Information File. Hence, no data is available for deposition in a repository system. Other data will be made available on request.

Acknowledgements

The financial support by the Dhaka University Research Grants financed by the University Grants Commission (UGC), Bangladesh provided through a research project is gratefully acknowledged. The authors are thankful to the Bangladesh Atomic Energy Commission, Dhaka and the Centre for Advanced Research in Sciences (CARS), University of Dhaka, for permitting the use of instrumental facilities for special characterization of the materials.

References

1 C. Xia, Y. Xia, P. Zhu, L. Fan and H. Wang, *Science*, 2019, **366**, 226–231.
2 S. C. Perry, D. Pangotra, L. Vieira, L.-I. Csepei, V. Sieber, L. Wang, C. Ponce de León and F. C. Walsh, *Nat. Rev. Chem.*, 2019, **3**, 442–458.
3 A. Huang, R. S. Delima, Y. Kim, E. W. Lees, F. G. L. Parlane, D. J. Dvorak, M. B. Rooney, R. P. Jansonius, A. G. Fink, Z. Zhang and C. P. Berlinguette, *J. Am. Chem. Soc.*, 2022, **144**, 14548–14554.
4 Y. Pang, H. Xie, Y. Sun, M.-M. Titirici and G.-L. Chai, *J. Mater. Chem. A*, 2020, **8**, 24996–25016.
5 Y. Sun, L. Silvioli, N. R. Sahraie, W. Ju, J. Li, A. Zitolo, S. Li, A. Bagger, L. Arnarson, X. Wang, T. Moeller, D. Bernsmeier, J. Rossmeisl, F. Jaouen and P. Strasser, *J. Am. Chem. Soc.*, 2019, **141**, 12372–12381.
6 Md. S. Hossain, Md. Y. Pabel and Md. M. Islam, in *Advanced Oxidation Processes in Dye-Containing Wastewater*, ed. S. S. Muthu and A. Khadir, Springer Nature Singapore, Singapore, 2022, pp. 29–89.
7 J. M. Campos-Martin, G. Blanco-Brieva and J. L. G. Fierro, *Angew. Chem., Int. Ed.*, 2006, **45**, 6962–6984.
8 P. Liu, H. Zhang, Y. Chen, Y. Di, Z. Li, B. Zhu, Z. Liu, Z. Zhang and F. Wang, *RSC Sustainability*, 2024, **2**, 483–490.
9 Z. Lu, G. Chen, S. Siahrostami, Z. Chen, K. Liu, J. Xie, L. Liao, T. Wu, D. Lin, Y. Liu, T. F. Jaramillo, J. K. Nørskov and Y. Cui, *Nat. Catal.*, 2018, **1**, 156–162.
10 H. Zhang, H. Xu, C. Yao, S. Chen, F. Li and D. Zhao, *ACS Nano*, 2024, **18**, 21836–21854.
11 Y. Gu, Y. Tan, H. Tan, Y. Han, D. Cheng, F. Lin, Z. Qian, L. Zeng, S. Zhang, R. Zeng, Y. Liu, H. Guo, M. Luo and S. Guo, *Nat. Synth.*, 2025, 1–8.
12 Y. Wu, Y. Zhao, Q. Yuan, H. Sun, A. Wang, K. Sun, G. I. N. Waterhouse, Z. Wang, J. Wu, J. Jiang and M. Fan, *Nat. Commun.*, 2024, **15**, 10843.
13 Y. Sun, L. Han and P. Strasser, *Chem. Soc. Rev.*, 2020, **49**, 6605–6631.

14 Md. S. Hossain, M. Y. A. Mollah, Md. A. B. H. Susan and Md. M. Islam, *Electrochim. Acta*, 2020, **344**, 136146.

15 T. I. Farhana, M. Y. A. Mollah, Md. A. B. H. Susan and Md. M. Islam, *Electrochim. Acta*, 2014, **139**, 244–249.

16 U. Martinez, J. H. Dumont, E. F. Holby, K. Artyushkova, G. M. Purdy, A. Singh, N. H. Mack, P. Atanassov, D. A. Cullen, K. L. More, M. Chhowalla, P. Zelenay, A. M. Dattelbaum, A. D. Mohite and G. Gupta, *Sci. Adv.*, 2016, **2**, e1501178.

17 J. Shui, M. Wang, F. Du and L. Dai, *Sci. Adv.*, 2015, **1**, e1400129.

18 H. He, S. Liu, Y. Liu, L. Zhou, H. Wen, R. Shen, H. Zhang, X. Guo, J. Jiang and B. Li, *Green Chem.*, 2023, **25**, 9501–9542.

19 X. Wu, Z. Yang, C. Li, S. Shao, G. Qin and X. Meng, *ACS Catal.*, 2025, **15**, 432–446.

20 Y. Xue, S. Sun, Q. Wang, Z. Dong and Z. Liu, *J. Mater. Chem. A*, 2018, **6**, 10595–10626.

21 F. Cheng, Y. Su, J. Liang, Z. Tao and J. Chen, *Chem. Mater.*, 2010, **22**, 898–905.

22 K.-Q. Ding, *J. Chin. Chem. Soc.*, 2009, **56**, 891–897.

23 T. Ohsaka, L. Mao, K. Arihara and T. Sotomura, *Electrochem. Commun.*, 2004, **6**, 273–277.

24 K. Sasaki, L. Zhang and R. R. Adzic, *Phys. Chem. Chem. Phys.*, 2008, **10**, 159–167.

25 M. D. S. Hossain and M. D. M. Islam, in *Renewable Polymers and Polymer-Metal Oxide Composites*, ed. S. Haider and A. Haider, Elsevier, 2022, pp. 45–77.

26 S. P. Deshmukh, A. G. Dhodamani, S. M. Patil, S. B. Mullani, K. V. More and S. D. Delekar, *ACS Omega*, 2020, **5**, 219–227.

27 C. Yuan, L. Su, B. Gao and X. Zhang, *Electrochim. Acta*, 2008, **53**, 7039–7047.

28 H. Wang, F. Yin, B. Chen and G. Li, *J. Mater. Chem. A*, 2015, **3**, 16168–16176.

29 Q. Tang, L. Jiang, J. Liu, S. Wang and G. Sun, *ACS Catal.*, 2014, **4**, 457–463.

30 K. A. Stoerzinger, M. Risch, B. Han and Y. Shao-Horn, *ACS Catal.*, 2015, **5**, 6021–6031.

31 A. Kulkarni, S. Siahrostami, A. Patel and J. K. Nørskov, *Chem. Rev.*, 2018, **118**, 2302–2312.

32 M. A. Hasan and M. M. Islam, *J. Energy Storage*, 2024, **98**, 113015.

33 Md. S. Hossain, A. Sahed, N. Jahan, M. Y. A. Mollah, Md. A. B. H. Susan and Md. M. Islam, *J. Electroanal. Chem.*, 2021, **894**, 115361.

34 R. Nissim, C. Batchelor-McAuley and R. G. Compton, *ChemElectroChem*, 2016, **3**, 105–109.

35 V. G. Khomenko, V. Z. Barsukov and A. S. Katashinskii, *Electrochim. Acta*, 2005, **50**, 1675–1683.

36 K. Q. Ding and F. M. Cheng, *Synth. Met.*, 2009, **159**, 2122–2127.

37 S. Vijayalakshmi, E. Kumar and S. Nithya, *Ionics*, 2020, **26**, 839–848.

38 R. Hoffmann, L. Strodtmann, K. Thiel, L. Sloboda, T. Urbaniak, A. N. Hubley and A. Hartwig, *Nano Sel.*, 2021, **2**, 271–292.

39 Z. Cao, L. Yang, H. Chen, C. Xu, D. Qi, S. Zhu and U. Ziener, *Colloid Polym. Sci.*, 2015, **293**, 277–288.

40 Md. Y. Bhat and S. A. Hashmi, *J. Solid State Electrochem.*, 2019, **23**, 591–606.

41 A. M. Hashem, A. E. Abdel-Ghany, R. El-Tawil, A. Bhaskar, B. Hunzinger, H. Ehrenberg, A. Mauger and C. M. Julien, *Ionics*, 2016, **22**, 2263–2271.

42 M. H. Alfaruqi, J. Gim, S. Kim, J. Song, J. Jo, S. Kim, V. Mathew and J. Kim, *J. Power Sources*, 2015, **288**, 320–327.

43 L. Feng, R. Wang, Y. Shi, H. Wang, J. Yang, J. Zhu, Y. Chen and N. Yuan, *Int. J. Electrochem. Sci.*, 2016, **11**, 5962–5972.

44 R. Yang, Z. Wang, L. Dai and L. Chen, *Mater. Chem. Phys.*, 2005, **93**, 149–153.

45 M. Setvín, U. Aschauer, P. Scheiber, Y.-F. Li, W. Hou, M. Schmid, A. Selloni and U. Diebold, *Science*, 2013, **341**, 988–991.

46 M. I. Hossain, T. Debnath, M. Y. A. Mollah, M. A. B. H. Susan and M. M. Islam, *RSC Adv.*, 2021, **11**, 10681–10687.

47 H. C. Zhou, J. R. Long and O. M. Yaghi, *Chem. Rev.*, 2012, **112**, 673–674.

48 M. Y. Pabel, A. Pandit, T. Taspya and M. M. Islam, in *Metal Phosphates and Phosphonates: Fundamental to Advanced Emerging Applications*, ed. R. K. Gupta, Springer International Publishing, Cham, 2023, 151–169.

49 D. N. G. Krishna and J. Philip, *Appl. Surf. Sci. Adv.*, 2022, **12**, 100332.

50 J. de A. Pereira, J. N. Lacerda, I. F. Coelho, C. de S. C. Nogueira, D. F. Franceschini, E. A. Ponzio, F. B. Mainier and Y. Xing, *Mater. Adv.*, 2020, **1**, 2433–2442.

51 J.-H. Jeong, J. W. Park, D. W. Lee, R. H. Baughman and S. J. Kim, *Sci. Rep.*, 2019, **9**, 11271.

52 X. Li, J. Li and F. Kang, *Ionics*, 2019, **25**, 1045–1055.

53 J. Yue and A. J. Epstein, *Macromolecules*, 1991, **24**, 4441–4445.

54 Y. Lee, C. Chang, S. Yau, L. Fan, Y. Yang, L. O. Yang and K. Itaya, *J. Am. Chem. Soc.*, 2009, **131**, 6468–6474.

55 N. A. Anastasijević, V. Vesović and R. R. Adžić, *J. Electroanal. Chem. Interfacial Electrochem.*, 1987, **229**, 305–316.

56 X. Chu, W. Yang and H. Li, *Mater. Horiz.*, 2023, **10**, 670–697.

57 S. Han, S. Park, S.-H. Yi, W. B. Im and S.-E. Chun, *J. Alloys Compd.*, 2020, **831**, 154838.

58 F. Wang, Y. Zheng, Q. Chen, Z. Yan, D. Lan, E. Lester and T. Wu, *Coord. Chem. Rev.*, 2024, **500**, 215537.

59 G. P. Hao, F. Hippauf, M. Oschatz, F. M. Wisser, A. Leifert, W. Nickel, N. Mohamed-Noriega, Z. Zheng and S. Kaskel, *ACS Nano*, 2014, **8**, 7138–7146.

60 H. Lv, Y. Song, Z. Qin, M. Zhang, D. Yang, Q. Pan, Z. Wang, X. Mu, J. Meng, X. Sun and X. X. Liu, *Chem. Eng. J.*, 2022, **430**, 133064.

61 L. Y. Dong, M. H. Guan, Y. Q. Ren, G. P. Hao and A. H. Lu, *Renewables*, 2023, **1**, 562–571.